Exploring the Atmosphere of Neoproterozoic Earth: The Effect of O_2 on Haze Formation and Composition

Sarah M. Hörst[1,2] ⓘ, Chao He[1] ⓘ, Melissa S. Ugelow[3], A. Mark Jellinek[4] ⓘ, Raymond T. Pierrehumbert[5] ⓘ, and Margaret A. Tolbert[2,3] ⓘ

[1] Department of Earth and Planetary Sciences, Johns Hopkins University, Baltimore, MD, USA; sarah.horst@jhu.edu
[2] Cooperative Institute for Research in Environmental Sciences, University of Colorado, Boulder, CO, USA
[3] Department of Chemistry and Biochemistry, University of Colorado, Boulder, CO, USA
[4] Department of Earth, Ocean and Atmospheric Sciences, University of British Columbia, Vancouver, BC, Canada
[5] Department of Physics University of Oxford Oxford, UK
Received 2018 February 14; revised 2018 April 4; accepted 2018 April 8; published 2018 May 15

Abstract

Previous studies of haze formation in the atmosphere of the early Earth have focused on $N_2/CO_2/CH_4$ atmospheres. Here, we experimentally investigate the effect of O_2 on the formation and composition of aerosols to improve our understanding of haze formation on the Neoproterozoic Earth. We obtained in situ size, particle density, and composition measurements of aerosol particles produced from $N_2/CO_2/CH_4/O_2$ gas mixtures subjected to FUV radiation (115–400 nm) for a range of initial $CO_2/CH_4/O_2$ mixing ratios (O_2 ranging from 2 ppm to 0.2%). At the lowest O_2 concentration (2 ppm), the addition increased particle production for all but one gas mixture. At higher oxygen concentrations (20 ppm and greater), particles are still produced, but the addition of O_2 decreases the production rate. Both the particle size and number density decrease with increasing O_2, indicating that O_2 affects particle nucleation and growth. The particle density increases with increasing O_2. The addition of CO_2 and O_2 not only increases the amount of oxygen in the aerosol, but it also increases the degree of nitrogen incorporation. In particular, the addition of O_2 results in the formation of nitrate-bearing molecules. The fact that the presence of oxygen-bearing molecules increases the efficiency of nitrogen fixation has implications for the role of haze as a source of molecules required for the origin and evolution of life. The composition changes also likely affect the absorption and scattering behavior of these particles but optical property measurements are required to fully understand the implications for the effect on the planetary radiative energy balance and climate.

Key words: astrobiology – Earth – planets and satellites: atmospheres

Supporting material: machine-readable tables

1. Introduction

The possible presence of an organic haze layer in the atmosphere of Archean Earth, similar to the one currently present in the atmosphere of Titan, has been suggested by a number of studies (see, e.g., Sagan & Chyba 1997; Pavlov et al. 2001a, 2001b; Domagal-Goldman et al. 2008; Haqq-Misra et al. 2008; Wolf & Toon 2010) and has been of particular interest as a factor in the resolution of the Faint Young Sun Paradox. Although, the effect of such a haze layer on climate would depend strongly on the altitude of the layer, the size, composition, and morphology of the particles, and the atmospheric gas composition as a haze layer could also cause an anti-greenhouse effect as it does on Titan (see, e.g., McKay et al. 1999; Haqq-Misra et al. 2008; Arney et al. 2016). It has also been used to explain measurements of sulfur isotopes (e.g., Domagal-Goldman et al. 2008). The climate of the Proterozoic presents a number of enigmatic features, including major glaciations at the beginning and end and a long period of apparent stasis in between (Pierrehumbert et al. 2011). Haze particles absorb and scatter light differently than gases and can therefore impact the temperature structure of an atmosphere. Atmospheric hazes can also serve as cloud condensation nuclei (CCN) and therefore can affect cloud formation (including size, altitude, and lifetime) and atmospheric albedo. Organic compounds present in atmospheric hazes are a source of material that may be useful for the origin and/or evolution of life (see, e.g., Hörst et al. 2012). To understand the role

atmospheres play in the habitability of a world and the origin of life, we must therefore understand the role of atmospheric hazes.

Atmosphere simulation experiments designed to investigate haze formation in the atmosphere of the early Earth have focused on an atmosphere that lacked molecular oxygen (O_2; see, e.g., Trainer et al. 2004, 2006; Nna-Mvondo et al. 2005; DeWitt et al. 2009; Hasenkopf et al. 2010; Fleury et al. 2015, 2017; Gavilan et al. 2017). Trainer (2013) provides an excellent review of our understanding of the atmosphere of the early Earth and previous early Earth experiments. Here, we present the results of a set of experiments that investigate the effect of O_2 on haze formation, particle size, and particle composition in $CH_4/CO_2/O_2/N_2$ atmospheres to understand haze formation during the rise of oxygen on the early Earth, the effect of abiotic O_2 on haze formation, and to begin thinking more broadly about the implications for the presence of a haze layer in the atmospheres of exoplanets where O_2 may be present.

2. Materials and Experimental Methods

2.1. Experimental Phase Space

A characteristic feature of present-day deep ocean hydrothermal vent plumes hosted in ultramafic rocks within the very slowly spreading parts of the mid-Atlantic ridge is a very large flux of abiotic CH_4 (e.g., Charlou et al. 1998). From experimental studies of olivine serpentinization (Janecky & Seyfried 1986; Berndt et al. 1996), the hydrothermal circulation
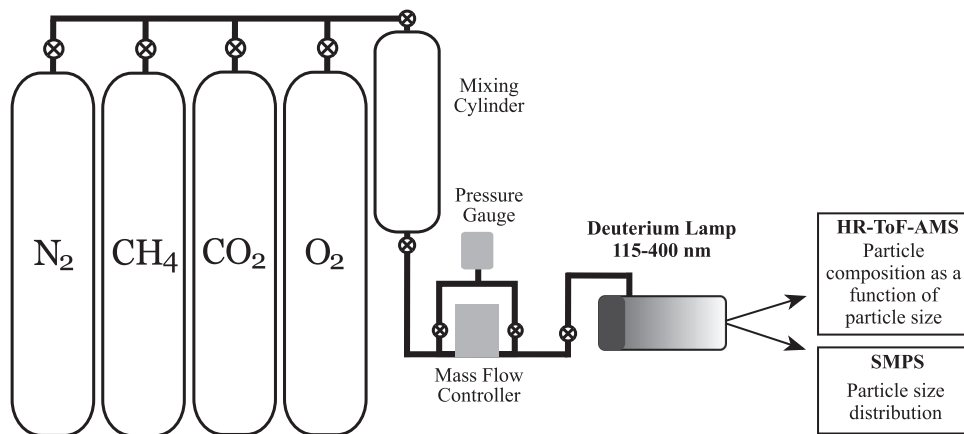
Figure 1. Shown here is a schematic of the experimental setup used for the experiments presented here. The gases mix overnight in a stainless steel mixing cylinder. Gases flow through the reaction cell where they are exposed to FUV photons from a deuterium lamp resulting in the formation of gas and solid phase products, which then flow out of the cell and into a high-resolution time-of-flight aerosol mass spectrometer (HR-ToF-AMS) or a scanning mobility particle sizer (SMPS). The HR-ToF-AMS measures particle composition as a function of particle size and the SMPS measures particle size distribution. All experiments presented here used a flow rate of 100 sccm and were run at room temperature and 620–640 torr (Boulder, Colorado, atmospheric pressure).

of seawater with dissolved CO_2 leads to the conversion of Fe (II) in olivine to Fe(III) in magnetite, and to the production of H_2 and the release of the observed CH_4 gas through "Fischer–Tropsch" reactions of the form

$$(Fe, \ Mg)_2SiO_4 \ + \ nH_2O \ + CO_2$$
$$= Mg_3Si_2O_5(OH)_4 + Fe_3O_4 + CH_4. \qquad (1)$$
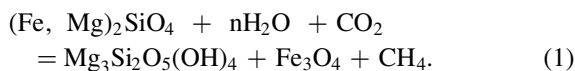
If the resulting flux of abiotic CH_4 into the deep ocean drives, in turn, a sufficiently large flux of CH_4 into the atmosphere this process can potentially lead to the production of organic hazes (see, e.g., Haqq-Misra et al. 2008).

The likelihood that such haze production will occur depends on the extent to which mantle rocks at mid-ocean ridges are involved in hydrothermal circulation and, in particular, on the residence time of CH_4 released into the deep ocean. In the oxygen-rich and biologically productive present-day ocean, little if any of this CH_4 is expected to escape to the atmosphere as the CH_4 that is not consumed by methanotrophs will be largely oxidized to CO_2. Furthermore, any remaining CH_4 that enters the atmosphere will be oxidized within only a few years to a decade. By contrast, a much larger fraction of this CH_4 is likely to exit the relatively low biomass Archean and Proterozoic oceans and enter into very low oxygen atmospheres with which they are in equilibrium (Lyons et al. 2014).

Methane released to the atmosphere before the Great Oxidation Event (2.4–2.1 Ga) ($O_2 < 10^{-6}$ PAL (present atmospheric level)) as well as during most of the Proterozoic ($10^{-3} < O_2 < 10^{-2}$ PAL) will have a residence time exceeding 10^3 years (Haqq-Misra et al. 2008). Constraining the magnitude of the CH_4 flux to the atmosphere even asymptotically is challenging. In particular, this flux will depend not only on the average rate of abiotic methane production but also on complex factors including the extent to which the ocean is fully oxygenated, on the full length and spreading rate of mid-ocean ridge compared to the present day, and the heights to which hydrothermal vent plumes penetrate stabilizing ocean density stratification, as well as their advection by ocean currents (e.g., Carazzo et al. 2013).

To explore the potential climate consequences of super-continental cycles in low O_2 worlds (such as neoproterozoic Earth and some extrasolar planets), we are interested in under-standing how the delivery of this abiotic methane affects haze

formation. We consequently chose initial gas concentrations to explore of possible CH_4/CO_2 ratios that result from the complex interplay between the mantle, crust, ocean, and atmosphere for O_2 concentrations relevant to Archean and Proterozoic Earths (Jellinek & Lenardic 2009; Lenardic et al. 2011; Jellinek et al. 2012). A broad range of O_2 concentrations were explored to understand the effect of O_2 on particle formation and composition, which has not been previously investigated.

We note here that there are possible biotic and abiotic sources for CH_4, CO_2, and even O_2, which can be produced at low concentrations by photochemistry (see, e.g., Kasting & Catling 2003; Wordsworth & Pierrehumbert 2014). It is for that reason we investigated a range of CH_4, CO_2, and O_2 concentrations to better understand their role in haze formation.

2.2. Haze Production Setup

A schematic of the experimental setup is shown in Figure 1. We introduced reactant gases (CH_4 99.99%), CO_2 (99.99%), O_2 (99.995%) Airgas) into a stainless steel mixing chamber that was then filled to 600 PSI with N_2 (99.999% Airgas). The gases mix for a minimum of 8 hr. During the experiments, reactant gases flow continuously through a glass reaction cell with a flow rate controlled by a Mykrolis FC-2900 mass flow controller and determined by instrument requirements (100 standard cubic centimeters per minute (sccm)). The pressure in the reaction cell is maintained between 620 and 640 torr at room temperature. As they flow through the reaction cell, the gases are exposed to a flux of FUV photons from a deuterium continuum lamp (Hamamatsu L1835, MgF_2 window, 115–400 nm). The flow continues out of the reaction cell and into either a scanning mobility particle sizer (SMPS) or a high-resolution time-of-flight aerosol mass spectrometer (HR-ToF-AMS).

The FUV photons initiate chemistry that results in the formation of aerosol in addition to gas-phase products. Although the photons produced by the deuterium lamp are not sufficiently energetic to directly dissociate N_2, we have demonstrated that nitrogen is participating in gas and solid phase chemistry occurring in our experiments (Trainer et al. 2012; Yoon et al. 2014; Hörst et al. 2018b), by an as of yet undetermined mechanism that likely involves CH_4 photolysis products (Trainer et al. 2012). Excited state atomic
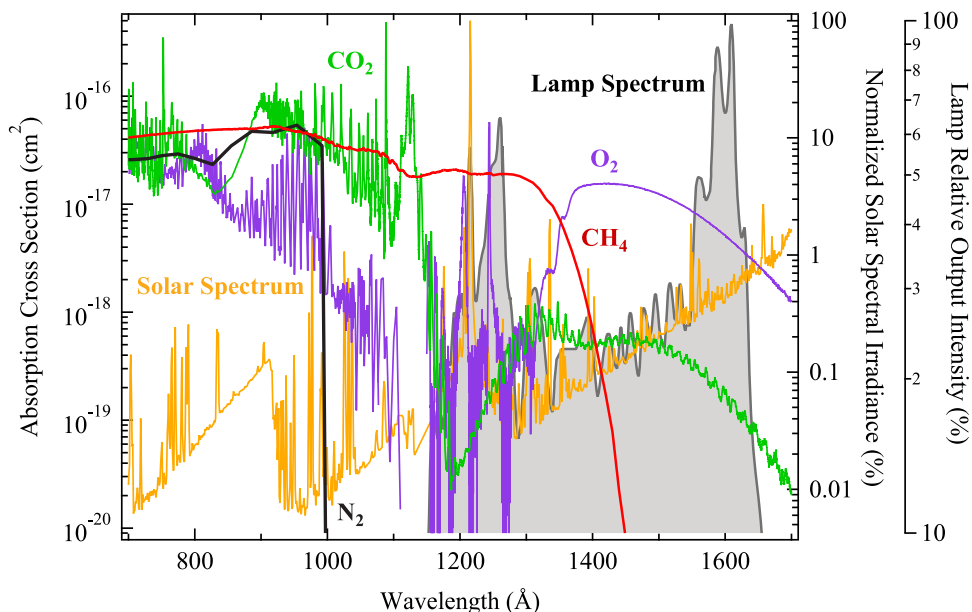
Figure 2. Shown here is a comparison of the absorption cross sections (left axis) of N_2 (black) (Chan et al. 1993), CH_4 (red) (Mount et al. 1977; Kameta et al. 2002; Chen & Wu 2004), CO_2 (green) (Huestis & Berkowitz 2010), and O_2 (purple) (Watanabe & Marmo 1956; Matsunaga & Watanabe 1967; Lu et al. 2010) to the solar spectrum (orange) (right, interior axis) (Woods et al. 2009) and the spectrum of the deuterium lamp used in these experiments (gray, filled) (right, exterior axis) (as provided by the manufacturer, Hamamatsu). Note that the N_2 cross section is highly structured, which is not captured in this simplified representation. There is a gap in the plotted cross sections for O_2 from 1110 to 1150 Å; the values are much lower than the other molecules in this region.

oxygen (e.g., $O(^1D)$) does not react with molecular nitrogen (Sander et al. 2006), and while O^+ can dissociate N_2 (Le Garrec et al. 2003), the photons used here are not sufficiently energetic to produce O^+ directly from O_2. Prasad & Zipf (2004, 2008) find that excited states of O_2 and O_3 can react with N_2 to produce odd nitrogen species; further work is necessary to ascertain if the mechanisms they suggest are possible under our experimental conditions. Figure 2 compares the lamp spectrum, solar spectrum, and cross sections of the molecules present in our initial gas mixtures.

Due to the reactive nature of the gas-phase products, in particular O_2 and its photolysis products, the stainless steel tubing connecting the reaction chamber to the instruments was replaced after each experiment. The lamp's MgF_2 window was cleaned using a 60/40 mixture (by volume) of acetone and methanol between each experiment. Both of these measures were implemented to ensure that if aerosol was deposited on surfaces in the experimental apparatus during one experiment, it did not participate in the chemistry of subsequent experiments. The chamber and lines were then pumped down overnight before running the experiment.

The instruments used to characterize the aerosol products of these experiments and data analysis techniques have been previously described by Hörst & Tolbert (2013) and Hörst et al. (2018b) (and references therein). Briefly, we use an HR-ToF-AMS (referred to hereafter as AMS; Aerodyne Research) to measure particle composition. The particles enter the AMS through a critical orifice (120 μm) and are then focused by an aerodynamic lens. The particles are flash vaporized at $\sim$600°C and the resulting molecules are ionized via 70 eV electron ionization. Analysis of the ions is performed with a high-resolution time-of-flight mass spectrometer (H-TOF platform, Tofwerk). The data presented here were collected using the W-mode of the HR-ToF-AMS, which has a longer flight path than the V-mode resulting in better mass resolution ($M/\Delta M \sim$3000–4300 for $m/z < 200$) but lower sensitivity DeCarlo et al. (2006). The AMS data were analyzed

using a combination of custom software and the AMS analysis software programs SQUIRREL and PIKA (DeCarlo et al. 2006; Aiken et al. 2007, 2008).

We use an SMPS (TSI) to measure the number of particles produced as a function of their mobility diameter. The SMPS ionizes the particles and then applies an electric field to the polydisperse aerosol and size selects the particles based on their electrical mobility against the drag force provided by a sheath flow. The size selected particles are then counted using light scattering measurements. The SMPS requires a higher flow rate than the HR-ToF-AMS, so an additional flow of N_2 (99.999% Airgas) was added after the reaction chamber to bring the total flow rate to 260 sccm. The additional flow was accounted for during data analysis.

For all gas mixtures (see Table 1), identical experiments were performed using the spark discharge from a Tesla coil as the energy source instead of the deuterium lamp (see, e.g., Hörst et al. 2018b). However, a detectable quantity of particles was not generated. The most likely reason for the lack of particle generation is that there is not a sufficient amount of CH_4 in the gas mixture. Previous work has shown that the optimum amount of CH_4 in CH_4/N_2 gas mixtures for particle production is 2% CH_4 in our setup using spark discharge to initiate chemistry (Hörst & Tolbert 2013). It is therefore not surprising that these experiments did not produce a detectable quantity of particles.

3. Results and Discussion

3.1. Production Rate, Particle Size, and Particle Number Density

Due to the complexities of multi-component gas mixtures, we first looked only at CH_4/N_2 and then at $CH_4/CO_2/N_2$ mixtures before adding O_2, as shown in Table 1. For the CH_4/N_2 mixtures, the production rate trend is consistent with previous work using our experimental setup (Trainer et al.

Table 1
Summary of Experiments

[CH₄]	CH₄	CH₄/CO₂ [CO₂]		CH₄/CO₂/O₂ [O₂]							
		260 ppm	394 ppm	2 ppm		20 ppm		200 ppm		2000 ppm	
20 ppm	AS										
79 ppm	AS	AS	AS	AS	AS	AS	AS	S	S	S	S
118 ppm	AS	AS	AS	AS	AS	AS	AS	AS	S	S	S
158 ppm	AS	AS	AS	AS	AS	AS	AS	AS	AS		

Note. The remaining gas is N_2, bringing the total to 100%. "S" indicates that measurements were made with the SMPS. "A" indicates that measurements were made with the HR-ToF-AMS. CO_2 is indicated by column color; experiments using 260 ppm CO_2 are light gray, and experiments using 394 ppm CO_2 are dark gray.

Table 2
SMPS Measurements

Column Number	Column Description
1	Diameter midpoint (nm)
2	19.7 ppm CH_4
3	78.8 ppm CH_4
4	78.8 ppm CH_4, 260 ppm CO_2
5	78.8 ppm CH_4, 260 ppm CO_2, 2 ppm O_2
6	78.8 ppm CH_4, 260 ppm CO_2, 20 ppm O_2
7	78.8 ppm CH_4, 260 ppm CO_2, 200 ppm O_2
8	78.8 ppm CH_4, 260 ppm CO_2, 2000 ppm O_2
9	78.8 ppm CH_4, 394 ppm CO_2
10	78.8 ppm CH_4, 394 ppm CO_2, 2 ppm O_2
11	78.8 ppm CH_4, 394 ppm CO_2, 20 ppm O_2
12	78.8 ppm CH_4, 394 ppm CO_2, 200 ppm O_2
13	78.8 ppm CH_4, 394 ppm CO_2, 2000 ppm O_2
14	118 ppm CH_4
15	118 ppm CH_4, 260 ppm CO_2
16	118 ppm CH_4, 260 ppm CO_2, 2 ppm O_2
17	118 ppm CH_4, 260 ppm CO_2, 20 ppm O_2
18	118 ppm CH_4, 260 ppm CO_2, 200 ppm O_2
19	118 ppm CH_4, 260 ppm CO_2, 2000 ppm O_2
20	118 ppm CH_4, 394 ppm CO_2
21	118 ppm CH_4, 394 ppm CO_2, 2 ppm O_2
22	118 ppm CH_4, 394 ppm CO_2, 20 ppm O_2
23	118 ppm CH_4, 394 ppm CO_2, 200 ppm O_2
24	118 ppm CH_4, 394 ppm CO_2, 2000 ppm O_2
25	158 ppm CH_4
26	158 ppm CH_4, 260 ppm CO_2
27	158 ppm CH_4, 260 ppm CO_2, 2 ppm O_2
28	158 ppm CH_4, 260 ppm CO_2, 20 ppm O_2
29	158 ppm CH_4, 260 ppm CO_2, 200 ppm O_2
30	158 ppm CH_4, 394 ppm CO_2
31	158 ppm CH_4, 394 ppm CO_2, 2 ppm O_2
32	158 ppm CH_4, 394 ppm CO_2, 20 ppm O_2
33	158 ppm CH_4, 394 ppm CO_2, 200 ppm O_2

Note. Table 2 is published in its entirety in the electronic edition of the *Astrophysical Journal*. A portion is shown here for guidance regarding its form and content. The units for columns 2–33 are $dN/dlogD_m$ (particles/cm³).

(This table is available in its entirety in machine-readable form.)

Table 3
HR-ToF-AMS Measurements

Column Number	Column Description
1	Mass/charge
2	19.7 ppm CH_4
3	78.8 ppm CH_4
4	78.8 ppm CH_4, 260 ppm CO_2
5	78.8 ppm CH_4, 260 ppm CO_2, 2 ppm O_2
6	78.8 ppm CH_4, 260 ppm CO_2, 20 ppm O_2
7	78.8 ppm CH_4, 394 ppm CO_2
8	78.8 ppm CH_4, 394 ppm CO_2, 2 ppm O_2
9	78.8 ppm CH_4, 394 ppm CO_2, 20 ppm O_2
10	118 ppm CH_4
11	118 ppm CH_4, 260 ppm CO_2
12	118 ppm CH_4, 260 ppm CO_2, 2 ppm O_2
13	118 ppm CH_4, 260 ppm CO_2, 20 ppm O_2
14	118 ppm CH_4, 394 ppm CO_2
15	118 ppm CH_4, 394 ppm CO_2, 2 ppm O_2
16	118 ppm CH_4, 394 ppm CO_2, 20 ppm O_2
17	158 ppm CH_4
18	158 ppm CH_4, 260 ppm CO_2
19	158 ppm CH_4, 260 ppm CO_2, 2 ppm O_2
20	158 ppm CH_4, 260 ppm CO_2, 20 ppm O_2
21	158 ppm CH_4, 394 ppm CO_2
22	158 ppm CH_4, 394 ppm CO_2, 2 ppm O_2
23	158 ppm CH_4, 394 ppm CO_2, 20 ppm O_2

Note. Table 3 is published in its entirety in the electronic edition of the *Astrophysical Journal*. A portion is shown here for guidance regarding its form and content. Column 1 is mass/charge. All other columns are intensity in arbitrary (but internally consistent) units.

(This table is available in its entirety in machine-readable form.)

2006; Hörst & Tolbert 2013), with an increase in production rate with increasing methane mixing ratio observed until the 158 ppm CH_4 case. The addition of CO_2 to the experiments decreases production rate and the effect is stronger for the 394 ppm case as shown in Figure 3. Given that the highest C/O ratio in our experiments was ∼0.8 this effect of CO_2 is consistent with the results of Trainer et al. (2004, 2006) even though these experiments use lower absolute CH_4 and CO_2 mixing ratios. At higher C/O ratios, the addition of CO_2 has been shown to increase the production rate (Trainer et al. 2004, 2006).

For all but the 260 ppm CO_2/158 ppm CH_4 case, the addition of 2 ppm O_2 increased the production rate, as shown by the increasing particle volume in the SMPS (Panel (A) of
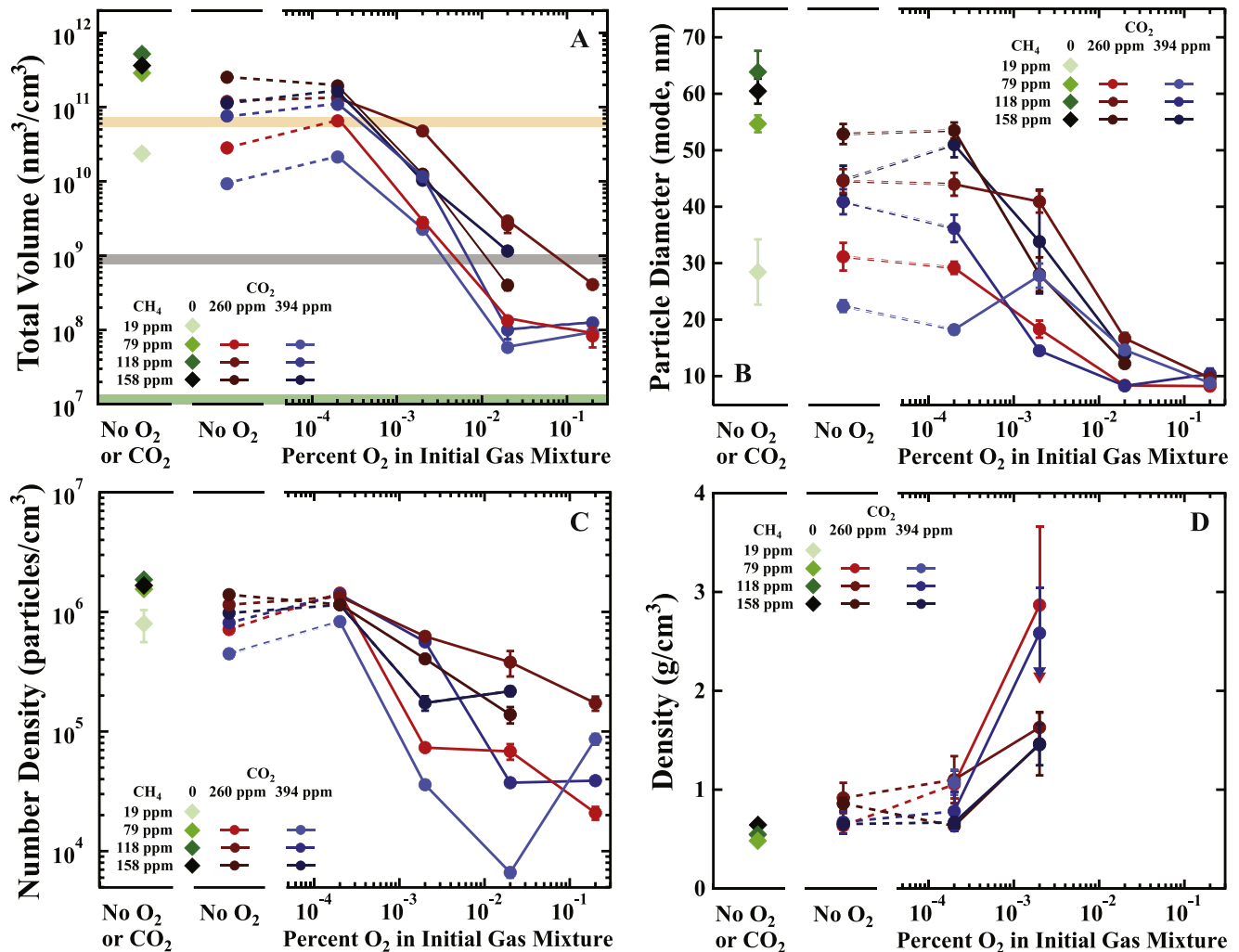
Figure 3. The total volume of particles produced for all of the experiments listed in Table 1 measured by the SMPS are shown in Panel (A). The shaded lines indicate the production rate from our standard Titan experiment using 0.1% CH_4 (Hörst & Tolbert 2013; Hörst et al. 2018b) (orange), laboratory air during one of the experimental runs (gray), and standard background measurement (the experiment running as usual, but without the lamp on) (green). Panel (B) shows the particle diameter and Panel (C) shows the number density of particles both from SMPS measurements. Panel (D) presents the particle density measurements obtained by combining SMPS and AMS data. The green points are for the CH_4/N_2 experiments, while the red and blue points indicate the experiments that contained 260 and 394 ppm CO_2, respectively.

Figure 3). However, the addition of more O_2 (20 ppm or greater) resulted in a decrease in aerosol production rate with increasing O_2 concentration. As demonstrated by the SMPS measurements, the observed trends in aerosol loading shown in Panel (A) of Figure 3 result from a decrease in particle diameter (Panel (B)) and a decrease in the number of particles (Panel (C)) with increasing O_2 concentration, indicating both nucleation and growth are affected by the inclusion of O_2 in the gas mixtures. As shown in Figures 3 (Panel (B)) and 4, as the O_2 concentration increases the particle diameter decreases, which has a few consequences for our measurements. First, it means that for our high oxygen concentration cases, we are likely missing part of the aerosol distribution at the small diameter end (e.g., the 0.2% O_2 size distribution in Figure 4) so the loading measurements shown in Figure 3 represent a lower limit. This will not be a large effect as it is the small radius end of the distribution that is missing. Second, there are implications for the density measurements, discussed below. The SMPS size distribution measurements for all experiments with sufficiently high production rates are available in Table 2.

Assuming the particles maintain the same optical properties, the transition to smaller particle size with increasing O_2 pushes the particles further into the Rayleigh scattering regime, where they will scatter shorter wavelengths more efficiently. Given the changes in composition discussed below, it is likely that the particles change both size and optical properties indicating that the effect on radiative transfer in the atmosphere will require measurement of optical constants and additional modeling to understand.

We would also like to note that we did not include H_2O in the initial gas mixture so that we could focus on the previously unexplored effect of O_2; however, models indicate that there may have been water at the 100 ppm level even in the stratosphere (Pavlov et al. 2000). To our knowledge, the effect of gas-phase H_2O in the absence of liquid water has not been experimentally explored previously with the exception of Hörst et al. (2018a), and He et al. (2018a, 2018b), who found that gas mixtures with substantial amounts of H_2O (55%–66%) were favorable for haze formation.
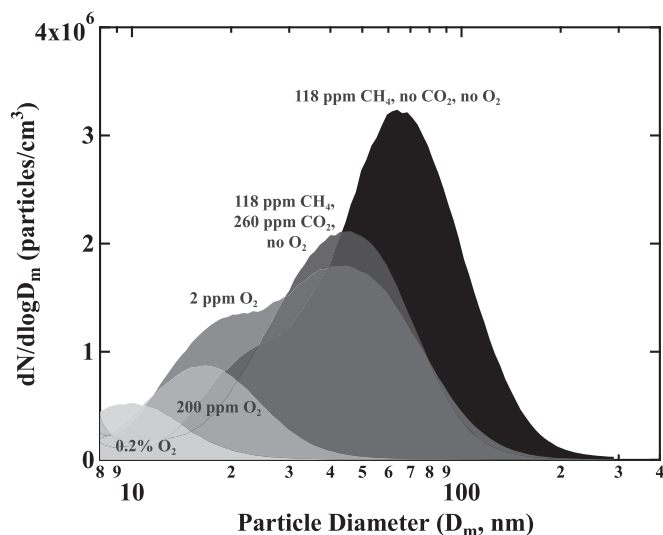
Figure 4. The size distributions for some of the 118 ppm CH_4 experiments measured by the SMPS are shown here. Of particular note is the bimodal distribution observed for the 2 ppm O_2 case. The SMPS size distribution measurements shown here and for all other experiments with sufficiently high production rates are available in Table 2.

The effect of oxygen-bearing species on photochemical haze generation is complicated by competing processes. While the addition of oxygen-bearing functional groups will terminate hydrocarbon chains (therefore often slowing or terminating growth) decreasing the solid production rate, the presence of oxygen-bearing functional groups also tends to lower the vapor pressure of species resulting in more efficient partitioning into the solid phase (see excellent discussion in Trainer et al. 2006). Further, H_2 has been shown to decrease haze production rates (Raulin et al. 1982; DeWitt et al. 2009; Sciamma-O'Brien et al. 2010) and the presence of oxygen-bearing species may serve to remove some H_2 from the system reducing that effect (see, e.g., Trainer et al. 2004, 2006; Hörst & Tolbert 2014; He et al. 2017; Hörst et al. 2018a).

Differences in the absorption cross sections of oxygen species, as shown for O_2 and CO_2 in Figure 2, further complicate identification of the mechanisms responsible for our observed changes. Both O_2 and CO_2 have larger absorption cross sections than CH_4 at longer wavelengths, and their presence could reduce photons that would otherwise be available to photolyze larger hydrocarbons and nitriles resulting in the production of larger molecules. At shorter wavelengths where CH_4 absorbs, CO_2 and O_2 also have cross sections that are competitive with CH_4, and thus their presence also likely decreases the efficiency of CH_4 photolysis. The decrease in CH_4 photolysis represents a decrease in the very first step of haze formation. These experiments were not designed to disentangle these different effects, but it is important to keep them in mind.

3.2. Particle Density

Particle density is an important parameter in cloud microphysics but is often set to one when modeling planetary hazes for simplicity and lack of any other constraints. Previous work has shown that this assumption may substantially overestimate particle density for Titan (Hörst & Tolbert 2013). Figure 3 (Panel (D)) shows particle density, which is calculated using a combination of size measurements from the SMPS (D_m) and

particle time-of-flight (PToF) mode of the AMS (D_{va}) as discussed extensively in DeCarlo et al. (2004) and Hörst & Tolbert (2013). Previous works have shown that the two diameters are related by effective particle density ρ_{eff},

$$\rho_{eff} = \rho_0 \frac{D_{va}}{D_m} = \rho_m S \qquad (2)$$

where ρ_0 is the unit density (1 g cm^{-3}), ρ_m is the material density of the particle, and S is the shape factor (Jimenez et al. 2003a, 2003b; DeCarlo et al. 2004).

At the small particle end of the size distribution, the SMPS and AMS differ in their ability to detect particles, with the SMPS being much more effective. The aerodynamic lens in the AMS transmits particles larger than 20 nm, but the greatest efficiency is for particles larger than 60 nm in diameter (Jayne et al. 2000). For this reason, Figure 3 does not have density measurements for the 200 ppm and 0.2% O_2 cases, even though particles were measured, because their size distributions were not reliably measured by the AMS. This is also responsible for the larger error bars for the 20 ppm O_2 cases. Note that for the 79 ppm CH_4, 20 ppm O_2 experiments, due to the AMS transmission efficiency, D_{va} is an upper limit and therefore the densities indicated are also upper limits. In general, particle densities increased with the addition of CO_2 as compared to the particles made only from N_2/CH_4 in the initial gas mixtures, and the densities further increased with the addition of O_2 to the experiments. This is consistent with the behavior observed in He et al. (2017) where density increased with increasing CO in the initial gas mixture indicating that particles with a higher weight percent of oxygen are more dense. He et al. (2017) note that their density increase was too large to be explained solely by the large molecular weight of the atomic oxygen compared to carbon, nitrogen, and hydrogen and could be related to other factors such as polarity resulting in increased intermolecular forces.

3.3. Particle Composition

Figure 5 shows the AMS measurements for the 158 ppm CH_4/260 ppm CO_2 experiments (shown at unit-mass resolution for simplicity). The processed HR-ToF-AMS measurements for all experiments with sufficiently high production rates are available in Table 3. The addition of CO_2 causes an obvious decrease in the relative amounts of benzene (78) and toluene (91). This decrease in aromatic molecule production is consistent with that observed by Trainer et al. (2006), which used larger concentrations of CH_4 and CO_2. This observation is particularly important given that aromatic molecules are efficient absorbers in the UV and visible, and experiments have shown that their presence impacts the absorption of haze analog particles in the far-infrared (Trainer et al. 2013; Sebree et al. 2014; Sciamma-O'Brien et al. 2017). Therefore the decrease in aromaticity may impact the optical properties.

The addition of CO_2 and then O_2 results in the formation of newly prominent peaks, which are most obvious in Figure 5 at mass 46, 60, and 73. The mass resolution of the HR-ToF-AMS is sufficient to allow for identification of the specific mass responsible for the changes measured at these peaks and the changes are attributed to increases in NO_2 (46) (see Figure 6), CH_4N_2O (60), and $C_2H_5N_2O$ (73), respectively. It is interesting to note that CH_4N_2O is the molecular formula for urea. NO (at mass 30) also increases with increasing O_2, although it does not stand out as strongly. The ratio of these peaks to the total
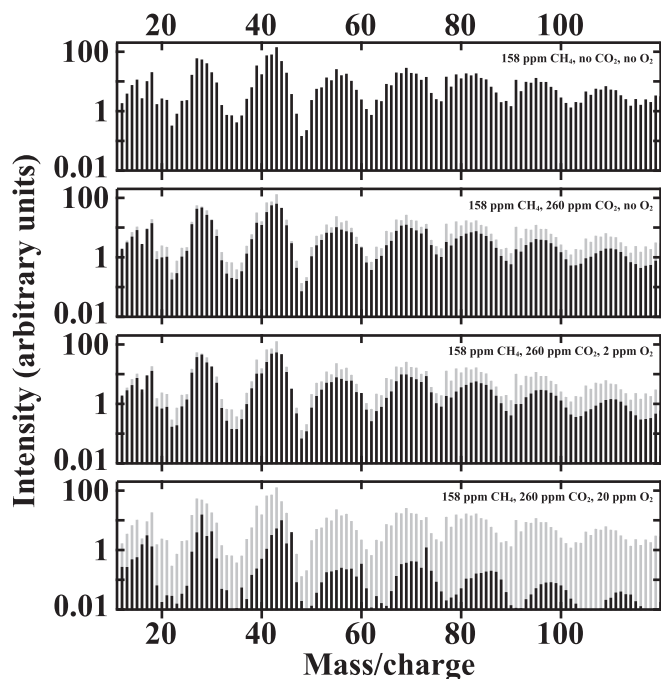
Figure 5. Here, we show how the HR-ToF-AMS measurements change with the addition of CO_2 and O_2 using the 158 ppm CH_4 and 260 ppm CO_2 cases. To facilitate comparison, the 158 ppm CH_4 measurements (top) are shown in gray with the rest of the measurements. The processed HR-ToF-AMS measurements shown here and for all other experiments with sufficiently high production rates are available in Table 3.
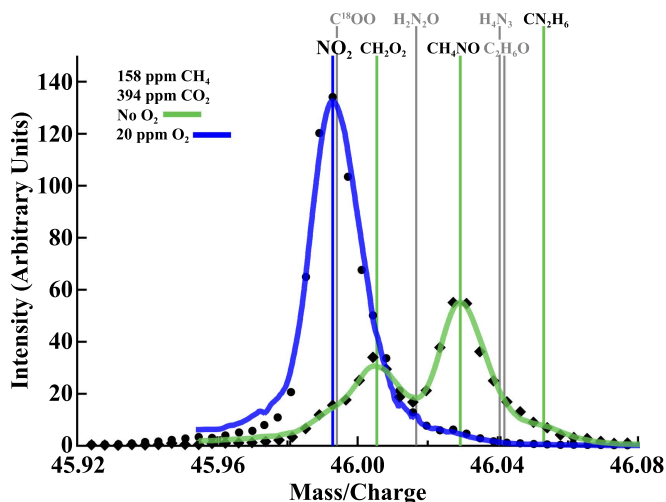

Figure 6. The HR-ToF-AMS has sufficient resolution and accuracy to differentiate between NO_2 and other molecules with the same nominal mass (46) as shown here. The thick green line shows the total fit to the data for the 158 ppm CH_4, 394 ppm CO_2 experiment, while the thick blue line shows the total fit when 20 ppm O_2 is added. The possible CHNO containing peaks with a nominal mass of 46 are also shown; those in gray were not used to fit the data from either experiment. The fit to the 20 ppm O_2 case includes only NO_2 (thick blue line). The fit to the no O_2 experiment includes NO_2, plus CH_2O_2, CH_4NO, and CN_2H_2. Note that although $C^{18}OO$ has almost the identical mass as NO_2, its abundance is constrained by the parent peak. Although the intensity here is in arbitrary units, the comparison between the two experiments is quantitatively valid.

organic signal is shown in Figure 7. The NO and NO_2 peaks likely result from fragmentation of nitrate-bearing molecules by the electron ionization system in the AMS (see, e.g., Farmer et al. 2010). It can be challenging to differentiate between
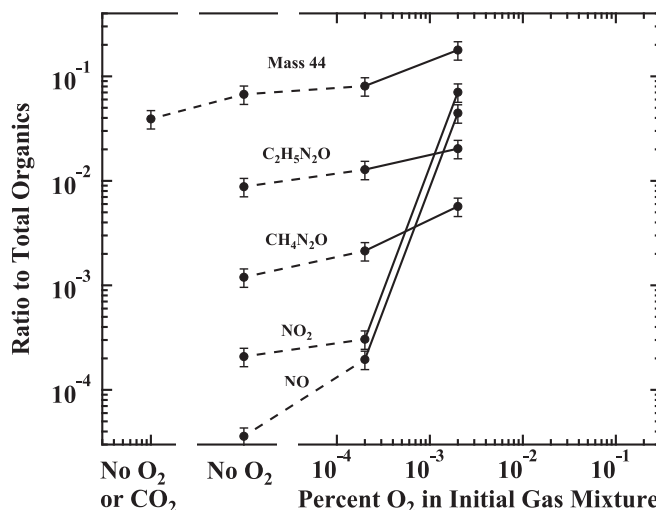

Figure 7. Shown here are the ratios of the mass 44 peak, NO, NO_2, CH_4N_2O, and $C_2H_5N_2O$ to the total organic content of the aerosol from AMS measurements for the 158 ppm CH_4 measurements shown in Figure 5.

organic and inorganic nitrate in the AMS and none of the methods explored by Farmer et al. (2010) appear to be appropriate for our data, presumably due to the very different types of aerosol investigated. The presence of numerous $C_xH_yN_zO_p^+$ ions indicates that some, if not all, of the observed nitrate is organic. Regardless of the final form, it is clear that the haze formation processes observed in these experiments are converting atmospheric N_2 to "fixed" nitrogen species, which are required for life and may have been the limiting nutrient during points in Earth's history (see discussion in Trainer 2013). Atmospheric production of fixed nitrogen is particularly interesting because it provides a global source, including a source of fixed nitrogen for Earth's oceans, as discussed previously by Yung & McElroy (1979) and Tian et al. (2011).

Previous work (see, e.g., Trainer et al. 2004) has used the peak at mass 44 as a proxy for degree of oxidation of organics in AMS measurements because of the presence of COO^+, which is a typical fragment of oxidized organic molecules. Indeed Figure 7 shows that the addition of CO_2, and then the addition of O_2, results in an increase of the ratio of mass 44 to the total organic signal, indicating that the aerosol becomes more oxidized. The increase in oxidation has implications both for the classes of compounds delivered to the surface and the optical properties of the haze particles. The trend observed with mass 44 is consistent with the overall elemental composition calculated from the AMS measurements. As shown in Figure 8, the addition of CO_2 and subsequent addition of O_2 results in an increase in the nitrogen content of the aerosol. This is true also of the oxygen content and it is at the expense of carbon. The elemental composition is also consistent with the increased abundance of nitrogen and oxygen containing compounds discussed above. Note that the error bars indicated in Figure 8 represent the error only on the reproducibility of the measurements. Extensive calibration of the HR-ToF-AMS with Earth atmosphere relevant compounds (Aiken et al. 2007, 2008) finds approximately 20% error on elemental ratios but the numbers were not reported for elemental percentages and are therefore not shown here.

The increased oxidation of laboratory haze analogues produced with CO_2 in addition to CH_4 affects their optical
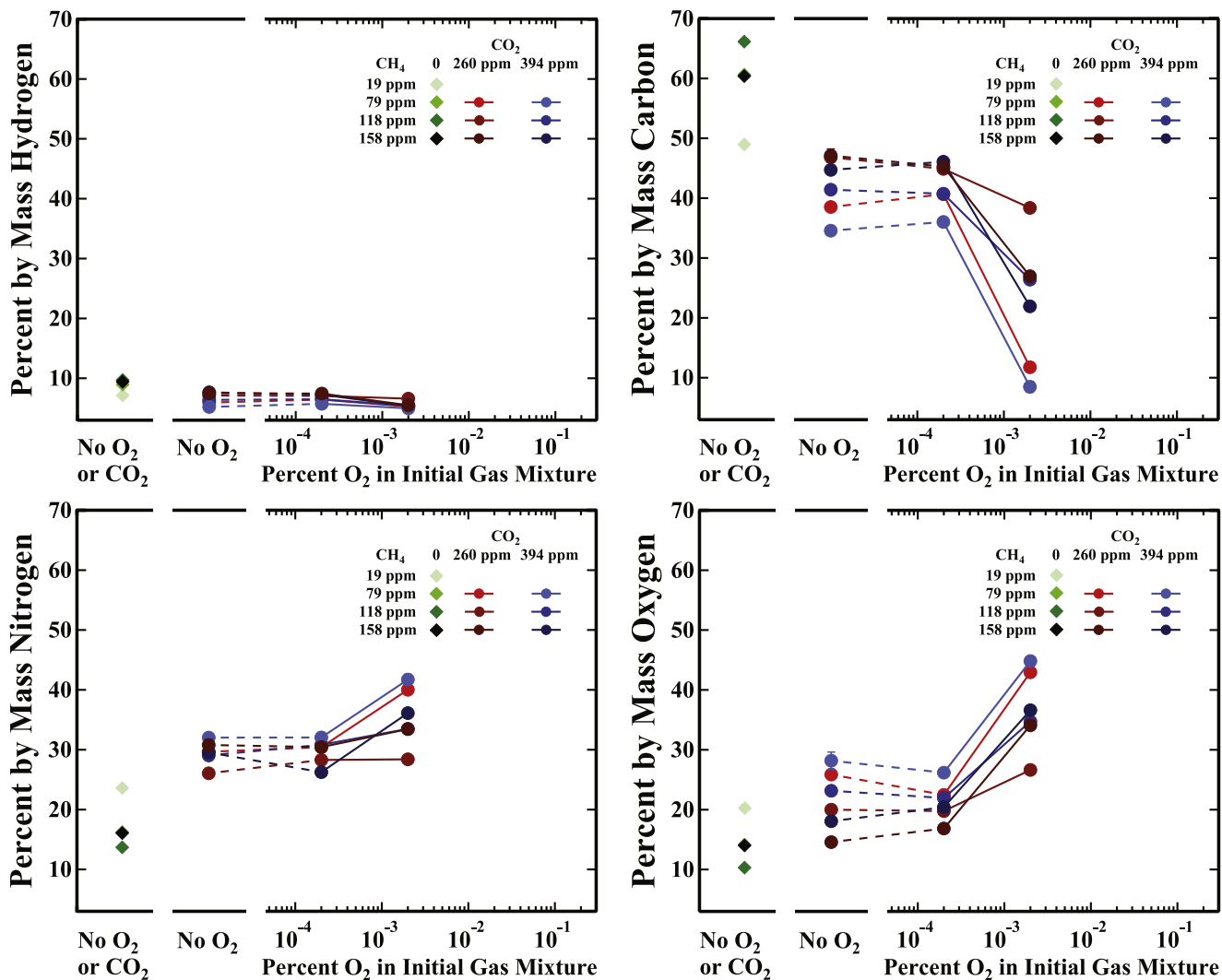
Figure 8. Shown here is the percent by mass of hydrogen, carbon, nitrogen, and oxygen in the aerosol particles as measured by the HR-ToF-AMS. Error bars are 1σ on the reproducibility of the measurements and are generally smaller than the symbol size. See the text for further error discussion.

properties, as shown by previous works. Hasenkopf et al. ([2010](#)) found a change in extinction at 532 nm when introducing CO_2 into CH_4/N_2 system resulting from an increase in the imaginary index of refraction. Gavilan et al. ([2017](#)) find similar results for analogues generated with a cold plasma in the UV wavelength region. However, as CO_2 is introduced in a 1:1 ratio with CH_4, the imaginary index of refraction actually decreases in the visible wavelength region that Gavilan et al. ([2017](#)) were able to model, which is the opposite of what is observed by Hasenkopf et al. ([2010](#)). Clearly more work is necessary to understand the effect of oxygen-bearing species on optical properties of haze particles.

4. Summary

Here, we investigated the effect of O_2 on haze formation and composition in laboratory atmosphere simulation experiments. For the smallest amount of O_2 (2 ppm) used, the addition resulted in an increase in particle production for all gas mixtures except one. However, at higher oxygen concentrations (20 ppm and greater), the addition of O_2 decreases the production rate of haze. As the amount of O_2 present in the

experiments increases, both the particle size and number of particles decreases, which indicates that O_2 affects particle nucleation and growth. Additionally, the density of the particles increases with increasing O_2. O_2 also affects the chemistry occurring in the chamber, resulting in measurable composition changes in the particle phase.

In terms of composition, the addition of the two oxygen-bearing species (CO_2 and O_2) not only increased the amount of oxygen in the aerosol, but it also increased the degree of nitrogen incorporation in the aerosol. In particular, the addition of O_2 resulted in the formation of nitrate-bearing molecules and other molecules that contain both nitrogen and oxygen. The fact that the presence of oxygen-bearing molecules increased the efficiency of nitrogen fixation has implications for the role of haze as a source of molecules required for the origin and evolution of life. In addition to the production of molecules that are potentially biologically interesting, the observed increase in oxidation state of the aerosol has a number of consequences for the transport of radiation in the atmosphere. For example, it is likely that the more oxidized aerosol is more hygroscopic and therefore a better CCN (see, e.g., Trainer [2013](#)), potentially affecting the atmospheric albedo due to

changes in clouds. The composition changes also likely affect the absorption and scattering behavior of these particles but measurements of the optical properties are required to fully understand the implications for the effect on radiative transfer.

Although the production rate decreases, the presence of modest amounts of O_2 does not fully suppress haze formation, and therefore its possible existence (including effects on climate and as a source of material to the surface) should not be neglected. We note that the sensitivity of the particle production rate to the abundances of the gases investigated here indicates the possibility that the existence of a haze layer and the properties of the haze particles present may have varied over time as the absolute and relative abundances of CO_2, CH_4, and O_2 varied.

ORCID iDs

Sarah M. Hörst ● https://orcid.org/0000-0003-4596-0702
Chao He ● https://orcid.org/0000-0002-6694-0965
Melissa S. Ugelow ● https://orcid.org/0000-0001-9725-6624
A. Mark Jellinek ● https://orcid.org/0000-0002-7372-7871
Raymond T. Pierrehumbert ● https://orcid.org/0000-0002-5887-1197
Margaret A. Tolbert ● https://orcid.org/0000-0001-5730-6412

References

Aiken, A. C., DeCarlo, P. F., & Jimenez, J. L. 2007, AnaCh, 79, 8350
Aiken, A. C., Decarlo, P. F., Kroll, J. H., et al. 2008, EnST, 42, 4478
Arney, G., Domagal-Goldman, S. D., Meadows, V. S., et al. 2016, AsBio, 16, 873
Berndt, M. E., Allen, D. E., & Seyfried, W. E., Jr 1996, Geo, 24, 351
Carazzo, G., Jellinek, A., & Turchyn, A. 2013, E&PSL, 382, 66
Chan, W., Cooper, G., Sodhi, R., & Brion, C. 1993, CP, 170, 81
Charlou, J. L., Fouquet, Y., Bougault, H., et al. 1998, GeCoA, 62, 2323
Chen, F., & Wu, C. 2004, JQSRT, 85, 195
DeCarlo, P., Slowik, J., Worsnop, D., Davidovits, P., & Jimenez, J. 2004, AerST, 38, 1185
DeCarlo, P. F., Kimmel, J. R., Trimborn, A., et al. 2006, AnaCh, 78, 8281
DeWitt, H. L., Trainer, M. G., Pavlov, A. A., et al. 2009, AsBio, 9, 447
Domagal-Goldman, S. D., Kasting, J. F., Johnston, D. T., & Farquhar, J. 2008, E&PSL, 269, 29
Farmer, D., Matsunaga, A., Docherty, K., et al. 2010, PNAS, 107, 6670
Fleury, B., Carrasco, N., Marcq, E., Vettier, L., & Määttänen, A. 2015, ApJL, 807, L29
Fleury, B., Carrasco, N., Millan, M., Vettier, L., & Szopa, C. 2017, E&PSL, 479, 34
Gavilan, L., Broch, L., Carrasco, N., Fleury, B., & Vettier, L. 2017, ApJL, 848, L5
Haqq-Misra, J. D., Domagal-Goldman, S. D., Kasting, P. J., & Kasting, J. F. 2008, AsBio, 8, 1127

Hasenkopf, C. A., Beaver, M. R., Trainer, M. G., et al. 2010, Icar, 207, 903
He, C., Hörst, S. M., Lewis, N. K., et al. 2018a, ApJL, 856, L3
He, C., Hörst, S. M., Riemer, S., et al. 2017, ApJL, 841, L31
He, C., Hörst, S. M., Yu, X., et al. 2018b, AJ, submitted
Hörst, S. M., He, C., Lewis, N. K., et al. 2018a, NatAs, 2, 303
Hörst, S. M., & Tolbert, M. A. 2013, ApJL, 770, L10
Hörst, S. M., & Tolbert, M. A. 2014, ApJ, 781, 53
Hörst, S. M., Yelle, R. V., Buch, A., et al. 2012, AsBio, 12, 809
Hörst, S. M., Yoon, Y. H., Ugelow, M. S., et al. 2018b, Icar, 301, 136
Huestis, D. L., & Berkowitz, J. 2010, Advances in Geosciences: Planetary Science (Singapore: World Scientific), 229
Janecky, D., & Seyfried, W., Jr. 1986, GeCoA, 50, 1357
Jayne, J., Leard, D., Zhang, X., et al. 2000, AerST, 33, 49
Jellinek, A., & Lenardic, A. 2009, JFM, 629, 109
Jellinek, M., Pierrehumbert, R., Turchyn, A. V., & Lenardic, A. 2012, AGU Fall Meeting 2012, T33J-06
Jimenez, J., Bahreini, R., Cocker, D., et al. 2003a, JGRD, 108, 4318
Jimenez, J., Bahreini, R., Cocker, D., et al. 2003b, JGRD, 108, 4733
Kameta, K., Kouchi, N., Ukai, M., & Hatano, Y. 2002, JESRP, 123, 225
Kasting, J. F., & Catling, D. 2003, ARA&A, 41, 429
Le Garrec, J., Carles, S., Speck, T., et al. 2003, CPL, 372, 485
Lenardic, A., Moresi, L., Jellinek, A., et al. 2011, GGG, 12, Q10016
Lu, H.-C., Chen, H.-K., Chen, H.-F., Cheng, B.-M., & Ogilvie, J. 2010, A&A, 520, A19
Lyons, T. W., Reinhard, C. T., & Planavsky, N. J. 2014, Natur, 506, 307
Matsunaga, F., & Watanabe, K. 1967, Sci. Light, 16, 31
McKay, C. P., Lorenz, R. D., & Lunine, J. I. 1999, Icar, 137, 56
Mount, G. H., Warden, E. S., & Moos, H. W. 1977, ApJL, 214, L47
Nna-Mvondo, D., Navarro-González, R., Raulin, F., & Coll, P. 2005, OLEB, 35, 401
Pavlov, A. A., Brown, L. L., & Kasting, J. F. 2001a, JGR, 106, 23267
Pavlov, A. A., Kasting, J. F., Brown, L. L., Rages, K. A., & Freedman, R. 2000, JGR, 105, 11981
Pavlov, A. A., Kasting, J. F., Eigenbrode, J. L., & Freeman, K. H. 2001b, Geo, 29, 1003
Pierrehumbert, R., Abbot, D., Voigt, A., & Koll, D. 2011, AREPS, 39, 417
Prasad, S. S., & Zipf, E. C. 2004, JGRD, 109, D08310
Prasad, S. S., & Zipf, E. C. 2008, JGRD, 113, D15307
Raulin, F., Mourey, D., & Toupance, G. 1982, OrLi, 12, 267
Sagan, C., & Chyba, C. 1997, Sci, 276, 1217
Sander, S. P., Friedl, R. R., Golden, D. M., et al. 2006, Chemical Kinetics and Photochemical Data for Use in Atmospheric Studies, Evaluation Number 15, Jet Propulsion Laboratory (Washington, DC: NASA)
Sciamma-O'Brien, E., Carrasco, N., Szopa, C., Buch, A., & Cernogora, G. 2010, Icar, 209, 704
Sciamma-O'Brien, E., Upton, K. T., & Salama, F. 2017, Icar, 289, 214
Sebree, J. A., Trainer, M. G., Loeffler, M. J., & Anderson, C. M. 2014, Icar, 236, 146
Tian, F., Kasting, J., & Zahnle, K. 2011, E&PSL, 308, 417
Trainer, M. G. 2013, Current Organic Chemistry, 17, 1710
Trainer, M. G., Jimenez, J. L., Yung, Y. L., Toon, O. B., & Tolbert, M. A. 2012, AsBio, 12, 315
Trainer, M. G., Pavlov, A. A., Curtis, D. B., et al. 2004, AsBio, 4, 409
Trainer, M. G., Pavlov, A. A., DeWitt, H. L., et al. 2006, PNAS, 103, 18035
Trainer, M. G., Sebree, J. A., Yoon, Y. H., & Tolbert, M. A. 2013, ApJL, 766, L4
Watanabe, K., & Marmo, F. 1956, JChPh, 25, 965
Wolf, E., & Toon, O. 2010, Sci, 328, 1266
Woods, T. N., Chamberlin, P. C., Harder, J. W., et al. 2009, GeoRL, 36, 1101
Wordsworth, R., & Pierrehumbert, R. 2014, ApJL, 785, L20
Yoon, Y. H., Hörst, S. M., Hicks, R. K., et al. 2014, Icar, 233, 233
Yung, Y. L., & McElroy, M. B. 1979, Sci, 203, 1002